PCCP

RSC Publishing

PAPER

View Article Online
View Journal | View Issue

Cite this: *Phys. Chem. Chem. Phys.*, 2013, **15**, 11717

Constructing inverse opal structured hematite photoanodes *via* electrochemical process and their application to photoelectrochemical water splitting†

Xinjian Shi,[a] Kan Zhang,[a] Kahee Shin,[a] Jun Hyuk Moon,[b] Tae-Woo Lee[c] and Jong Hyeok Park*[ad]

Received 31st January 2013,
Accepted 13th May 2013

DOI: 10.1039/c3cp50459j

www.rsc.org/pccp

In this study, we constructed an inverse opal structured hematite (IOS α-Fe_2O_3) as the photoanode of a photoelectrochemical (PEC) cell for efficient solar water splitting *via* a simple electrochemical process. At the same time, a series of affecting factors (template particle size, electrodeposition time and annealing temperature) to construct the IOS α-Fe_2O_3 photoanode on the photoelectrochemical water splitting were considered. Optimized PEC efficiency was observed for the IOS α-Fe_2O_3 photoanode annealed at 400 °C using the 250 nm sized-polystyrene (PS) colloid template and 9 minutes of electrodeposition time for the given specific Fe precursor solution. This resulted in the highest photocurrent density compared to other crossed conditions, which significantly achieved 3.1 mA cm^{-2} at 0.5 V *vs.* Ag/AgCl reference electrode. The synthesis of the IOS α-Fe_2O_3 *via* an easy-to-control electrochemical process is described for first time that opens a possibility for constructing other oxide semiconductor photoanodes (not only well-known Si, Ti and Zr) with inverse opal structure.

Introduction

Nowadays, hydrogen has received much attention as a next-generation energy carrier for the future. Because solar splitting of pure water into H_2 and O_2 can be easily carried out by photo-assistance processes alone, it has been considered as a kind of clean and renewable energy source for hydrogen generation.[1–5] Since Fujishima and Honda's report on photoelectrochemical (PEC) water splitting using a titanium dioxide (TiO_2) semiconductor photoanode in 1972, solar hydrogen production by water splitting from n-type semiconductors has been considered one of the best ways to convert a naturally abundant and benign substance into an energy source.[2] Among the various semiconductor photoanode materials, hematite (α-Fe_2O_3) with a relatively narrow band gap, widespread availability, chemical stability and most importantly, low cost and abundance, makes it an attractive material for PEC water splitting under solar illumination.[6–12] Although PEC water splitting using α-Fe_2O_3 holds a promising approach for hydrogen production, some drawbacks, such as the short carrier diffusion length and poor electric conductivity, still limit its optimal contribution.[13,14] To solve the aforementioned problems, doping of α-Fe_2O_3 by metal ions appears to be an efficient approach for the enhancement of carrier diffusion and electric conductivity;[15–22] however, it was a well-known fact that metal doped α-Fe_2O_3 suffers from low thermal stability during the annealing process at high temperature.

Controlling of the nanostructure of α-Fe_2O_3 was believed to be another possible technology for overcoming the disadvantages of α-Fe_2O_3 due to mechanism-dependent semiconductor geometric structure. For instance, different kinds of α-Fe_2O_3 geometric structures, such as mesoporous,[8] nanorod,[23–25] nanotube,[26] nanobelt,[10] nanowire,[7] and ultrathin sheet,[27] demonstrated enhancement of photoactivity performance compared to general α-Fe_2O_3 particles or films. Most recently, three-dimensionally ordered macroporous structured photoanodes (inverse opal) with substantially increased surface area have been constructed for the improvement of electron transport and light harvesting due to the remarkably increased optical path length by multi-scattering.[28–34] It is surprising that the artificial inverse opaline structure having the skeleton surrounding uniform close-packed

[a] *School of Chemical Engineering, Sungkyunkwan University, Suwon 440-746, Republic of Korea. E-mail: lutts@skku.edu*
[b] *Department of Chemical and Biomolecular Engineering, Sogang University, 1 Shinsu-dong, Mapo-gu, Seoul 121-742, Korea*
[c] *Department of Materials Science and Engineering, Pohang University of Science and Technology, San 31, Hyoja-dong, Nam-gu, Pohang, Gyeongbuk 790-784, Korea*
[d] *SKKU Advanced Institute of Nanotechnology (SAINT), Sungkyunkwan University, Suwon 440-746, Republic of Korea*

† Electronic supplementary information (ESI) available. See DOI: 10.1039/c3cp50459j

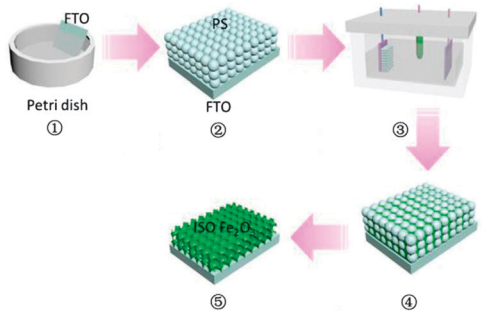

Fig. 1 The schematic diagram of the template-assisted electrodeposition method process to fabricate an inverse opal structured α-Fe_2O_3: ① FTO immersed into PS colloid for 2 days; ② polystyrene beads on FTO (250, 500, 900 nm beads); ③ Fe electrodeposition by a three-electrode system (5, 9, 12 minutes); ④ the iron growth in the PS beads gap; ⑤ inverse opal structured α-Fe_2O_3 generation after annealing (300, 350, 400, 500 °C).

macropores with a face-centered-cubic (FCC) structure provided high specific surface area and porosity, as well as an additional photonic bandgap effect to enhance the light–matter interactions.[35–38] Even though IOS semiconductors have successfully been used in dye-sensitized solar cells, PEC and photocatalysis,[27–34,39–42] limitation of starting materials as a "bottleneck" still needs to be overcome to expand their practical applications.

In this work, we report for the first time on the construction of the IOS α-Fe_2O_3 as a photoanode *via* a simple electrochemical process for PEC water splitting. The electrochemical deposition method for formation of the IOS α-Fe_2O_3 was demonstrated here by a stacking of PS nanobeads on the FTO substrate, followed by iron electrodeposition and high temperature sintering in air, as schematically illustrated in Fig. 1. PEC activity of the IOS α-Fe_2O_3 was optimized by varying parameters, such as template particle size, electrodeposition time and annealing temperature. As far as we know, no previous work has been reported regarding the IOS α-Fe_2O_3 as the photoanode in PEC water splitting.

Experimental

Preparation of different sized PS colloidal film on FTO

The different sized polystyrene (PS) colloids were prepared by the emulsifier-free emulsion polymerization method. We made mainly three sizes (250, 500 and 900 nm) of PS colloidal particles which were dependent on the synthesis temperature, the composition of the reaction mixture, and the kind of solvent used.[43,44] For example, 900 nm PS colloidal particles were synthesized by using styrene (Showa, 98%) as the monomer, potassium persulfate (Aldrich) as the initiator, potassium bicarbonate (Sigma) as the buffer and sodium styrene sulfonate (Aldrich) as the comonomer. To assemble three-dimensional (3D) colloidal crystals, ethanol was used as a dispersing solvent. Besides, ethanol and acetone mixture was used to clean the fluorine-doped tin oxide (FTO, TEC-8, Pilkilton) glass substrates with sonication for 20 minutes. Then FTO glass was put into the miscible liquor of sulfuric acid and hydrogen peroxide for 15 minutes to make their surfaces hydrophilic. The surface treated FTO glass was immersed into the PS colloidal suspensions, and placed in the oven at 50 °C for two days. To form uniform PS beads, the weight percent of PS in colloidal solution was controlled at 0.15 wt%. Total 20 ml PS colloidal solution was then put in the petri dish placed with tilted FTO glass inside. The PS thin films coated on the FTO glass can be obtained after evaporation of the solvent. Usually the thickness of PS used in experiment is around 13 μm (Fig. S1d, ESI†).

Synthesis of inverse opal and general structured α-Fe_2O_3

Chemicals for Fe electrodeposition were based on the procedure reported previously,[9,26] which included ferrous sulfate ($FeSO_4 \cdot 7H_2O$, 98.0%, Junsei Chemical Co. Ltd), ascorbic acid ($C_6H_8O_6$, 99%, Sigma Aldrich), amidosulfonic acid (H_2NSO_3H, 99.99%, Sigma Aldrich) and boric acid (H_3BO_3, 99.99%, Sigma Aldrich). Hydrophilic PS surface was achieved by oxygen plasma treatment for 90 seconds. Iron was reductively grown by an electrochemical method onto the PS/FTO from the stable Fe^{2+} salt solution. After 5, 9 and 12 minutes of electrodeposition, the samples prepared were thermally annealed in air atmosphere to oxidize iron and remove the polymer template at 300, 350, 400 and 500 °C for 6 hours, respectively. For general structured α-Fe_2O_3 (as control group), the electrodeposition process was conducted by depositing iron on a pure clean FTO rather than PS template. The best conditions which are the same as the inverse opal structure were applied (9 minutes iron growth and 400 °C annealing).

Characterizations

To obtain the images of the prepared colloidal crystals and their inverted structures, field emission scanning electron microscopy (FESEM, JSM-7000F, Japan) was used. All samples were coated with Pt to improve the conductivity before SEM. The crystalline phase was checked with a Siemens diffractometer D500/5000 in Bragg–Bretano geometry with Cu Kα radiation. X-ray photoelectron spectroscopy (XPS) measurements were carried out by an AESXPS instrument (ESCA2000 from VG Microtech in England) equipped with an aluminum anode (Al Kα = 1486.6 eV).

The photocurrent–voltage (*I–V*) behaviours were measured by using a three-electrode system in which we used Ag/AgCl as the reference electrode, Pt plate as the counter electrode and 1 M NaOH as the electrolyte. A potentiostat (CH Instruments, CHI 660) was used to control the potential and other parameters. 1.5 cm × 1.0 cm active material was electrodeposited on top of the FTO substrate whose size is 1.5 cm × 1.5 cm. Then the irradiated area of sample which has been retained at 25 mm^2 by imide tape coverage was examined under AM 1.5 G sunlight of 100 mW cm^{-2} by solar simulator irradiation (PECCELL, Yokohama, Japan, PEC-L01). A silicon reference cell (Fraunhofer ISE, Certificate No.C-ISE269) was used to calibrate its light intensity. The incident photon-to-current efficiency (IPCE) data was obtained by using a monochromator (Polaronix K3100 IPCE Measurement System, McScience) with a 300 W xenon light source. The impedance curve was checked by the same CHI machine under AM 1.5 G light illumination from a solar simulator, with the A.C. impedance mode.

Results and discussion

The IOS α-Fe_2O_3 formed from different sized PS sphere templates were observed by the top view of FE-SEM (Fig. 2a–c), which revealed ordered periodicity and wide pore interconnectivity. The diameters of these inverse opals are *circa* 215, 418 and 806 nm corresponding to 250, 500 and 900 nm sized PS colloid templates (Fig. S1a–c, ESI†), respectively. It was obvious that the hole size of the inverse opals was significantly reduced by a minimum of 15% compared to that of the original PS sphere templates, which could be ascribed to the shrinkage of the structure during the growth of α-Fe_2O_3.

The thickness variation of IOS α-Fe_2O_3 as a function of electrodeposition time for iron was also characterized by the cross section of FE-SEM, as shown in Fig. 2d–f. It can be clearly seen that the increased thickness of α-Fe_2O_3 thin film from 5 μm to over 10 μm could be easily controlled by adjusting electrodeposition time from 5 to 12 minutes. Moreover, the inverse opals structure could be uniformly formed as seen from the cross-section view, which is beneficial to unhindered electrolyte infiltration throughout the entire thickness of the α-Fe_2O_3 photoanode.

The photocurrent densities of the IOS α-Fe_2O_3 photoanodes with different hole sizes are firstly evaluated at a potential region between −0.4 and 0.8 V under dark and simulated solar light illumination, as shown in Fig. 3a. Compared to the dark condition, the photocurrent densities of the IOS α-Fe_2O_3 photoanodes show pronounced enhancement when it was illuminated with solar light, which implies efficient light harvesting of α-Fe_2O_3. Typically, the photocurrent increases from the onset potential of approximately 0.15 V *vs.* Ag/AgCl electrode and approaches a plateau at around 0.5 V *vs.* Ag/AgCl electrode. The maximum photocurrent density calculated *vs.* per square centimetre is 3.1 mA for the 250 nm-diameter photoanode (the sample area used for calculating is projected geometric electrode area). A previous study by Kwak *et al.* indicated a decrease of solar conversion efficiency with size reduction.[28] As it is well-known, the inverse opal with a replicated shell structure of an fcc opal offers a very high specific surface area and porosity, which are crucial for enhancement of photocurrent density.[35–38] This means small sized spheres will have a larger surface area than

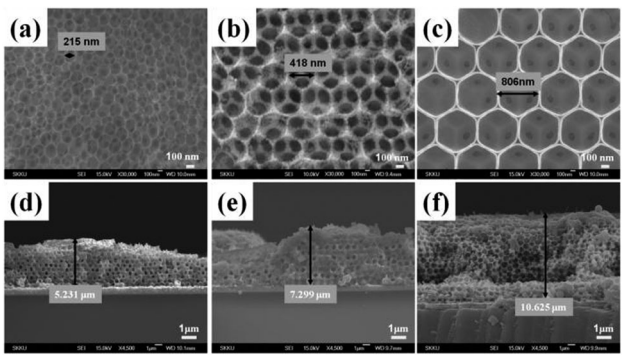

Fig. 2 The top view of different template particle size samples which are annealed at 400 °C: (a) 250; (b) 500 and (c) 900 nm; the cross-sectional view of different deposition time samples: (d) 5; (e) 9 and (f) 12 minutes.

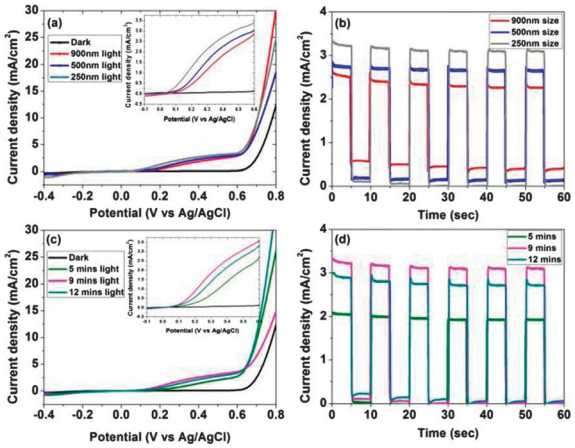

Fig. 3 The photocurrent behaviors of different template particle size samples in 1 M NaOH electrolyte under AM 1.5 G light with 9 minutes electrodeposition time under 400 °C annealing (a) *vs.* potential and (b) *vs.* time (0.5 V *vs.* Ag/AgCl); the photocurrent behaviours of different deposition time samples made by 250 nm beads under 400 °C annealing: (c) *vs.* potential and (d) *vs.* time (0.5 V *vs.* Ag/AgCl).

larger spheres if they have the same space volume, thus the smaller spheres would have more exposed area after their removal to form an inverse opal structure. Besides, the different electrodeposition time can determine different thickness directly as seen in Fig. 2d–f. Several literature reports have mentioned the relationship between sample thickness and the indirect band gap.[45–47] Here the indirect band gaps were roughly calculated from absorbance of UV-Vis reflectance spectrum (shown as Fig. S2, ESI†) by using the transformed Kubelka–Munk function. A shorter bandgap is conducive to the photonic capture in a wide range of wavelengths, however, the longer diffusion length will simultaneously cause more charge recombination before electrons reach the FTO surface. Taking into account these two opposing factors, it can be explained that the moderate thickness (7 μm) sample shows the best photoelectrical behaviour.

Annealing temperature, as another important parameter, can induce different crystalline orders and defects during the conversion of Fe to α-Fe_2O_3, which closely relates to the photoelectrochemical properties.[7,8] The *I–V* curves of the IOS α-Fe_2O_3 with annealing for 6 h at temperatures ranging from 300 °C to 500 °C are shown in Fig. 4a (the PS template can be well removed at over 400 °C which is confirmed by Fig. S3, ESI†).

It was observed from Fig. 4a that a slight increase in photocurrent density up to the annealing temperature of 400 °C, followed by a sudden decrease when the annealing temperature increased to 500 °C. These temperature-dependent results are well matched with the previous reports by Hahn *et al.*[48] Regretfully, the researchers did not give a plausible explanation as to why higher crystalline order and lower defect obtained at 500 °C resulted in the lower photocurrents. Because of this, it was meaningful for us to do the following work. A similar phenomenon could be observed in the IOS α-Fe_2O_3 case, for which the XPS spectra of the IOS α-Fe_2O_3 with different annealing temperatures were firstly investigated, as shown in Fig. 4b. The binding energies of Fe 2p 3/2 and Fe 2p 1/2 were located at 711.0 eV and 725.0 eV, respectively,

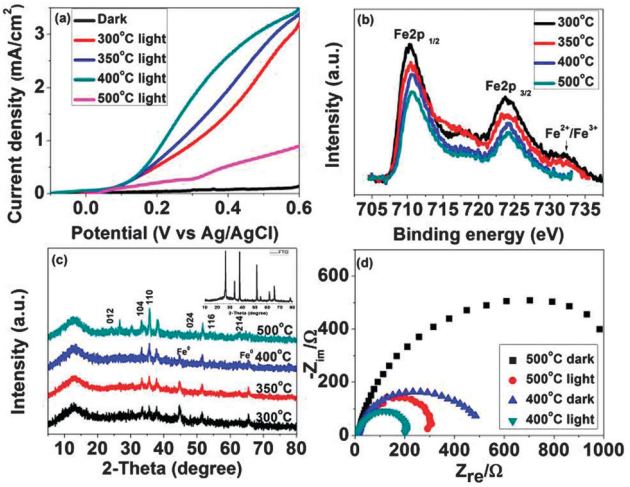

Fig. 4 The characterization diagram and spectrum of different annealing temperature samples made by 250 nm beads with 9 minutes electrodeposition time: (a) the photocurrent behaviors *vs.* potential in 1 M NaOH electrolyte under AM 1.5 G light; (b) X-ray photoelectron spectroscopy; (c) X-ray diffraction pattern; (d) electrochemical impedance spectroscopy (EIS) Nyquist plots.

which was for Fe^{3+} in α-Fe_2O_3.[49,50] A notable hump at 732.3 eV in the IOS α-Fe_2O_3 with annealing temperatures at 300 and 350 °C was present, which could be ascribed to unconverted Fe^{2+}/Fe^{3+} (shake up satellites).[51] This result confirms a crystalline defect of the IOS α-Fe_2O_3 occurring at 300 and 350 °C relevant to lower photocurrent density as compared with that of the IOS α-Fe_2O_3 at 400 °C. However, it is still difficult to explain the reason of the rapidly decreasing photocurrent over the IOS α-Fe_2O_3 at 500 °C.

The XRD pattern of the IOS α-Fe_2O_3 was carried out which also showed an obvious increase in the intensity of diffraction peaks with the annealing temperature ranging from 300 to 500 °C, indicating a fine formation of crystalline order at 500 °C (Fig. 4c).

Our previous works reported that the α-Fe_2O_3 nanorod or nanotube structured electrodes have high photocurrent density at an annealing temperature of 500 °C using the hard template assisting growth method.[9,26,52] Whereas, considering the formation of the IOS α-Fe_2O_3 originating from the soft PS template, the final morphology of α-Fe_2O_3 might be significantly influenced by different annealing temperatures. For the purpose of comparison, the SEM images of the IOS α-Fe_2O_3 at 400 °C and 500 °C were checked, as shown in Fig. 5. It could be clearly seen that the fcc opals were well represented in the IOS α-Fe_2O_3 at 400 °C, while no such structure was present in the IOS α-Fe_2O_3 at 500 °C (the holes of the 500 °C sample were in the state of the uneven and mutual extruding growth). Presumably, higher temperature will result in a more rapid formation of α-Fe_2O_3 from Fe, which leads to the distortion in the geometry of the inverse opal structure. Moreover, the walls of IOS α-Fe_2O_3 prepared at 500 °C have changed to interconnected nanoparticle-like morphology, resulting in increased charge transportation. These phenomena might occur in the α-Fe_2O_3 thin film PEC.[48] However, this behavior is more obvious in the IOS α-Fe_2O_3 system. The change

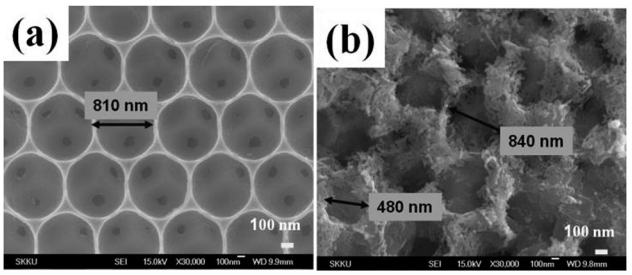

Fig. 5 The surface pore structure (SEM) comparison of samples made by 900 nm beads with 9 minutes electrodeposition time under different annealing temperatures: (a) 400 °C; (b) 500 °C.

of the geometry would be reflected in electrochemical resistance characteristics.[53–55] As shown in Fig. 4d, the arc diameter in the Nyquist plot of the IOS α-Fe_2O_3 at 400 °C electrode is smaller than that of the IOS α-Fe_2O_3 at 500 °C electrode under both dark and irradiated conditions. The smaller arc diameter indicates a lower resistance of the interfacial charge transfer.[56] In addition, the Nyquist plot under a dark condition can also indicate that the distortion in the geometry of the inverse opal structure is detrimental for charge transfer and electrolyte infiltration. We believe that the present work reminds us of an issue which has always been ignored: the preparation condition relevant to the geometry of the electrode may have a huge effect on photoelectrochemical properties. A large number of previous literature reports often gave some controversial results on the photoactivity of one componential catalyst in similar reactions. Therefore, in this case, the role of temperature has been carefully investigated, and we reasonably inferred that the varying geometries relative to different temperatures can result in the change of photoelectrochemical properties.

Finally, in order to clarify the advantages of inverse opal structure, the general structured α-Fe_2O_3 (planar film) was fabricated as a control group, whose SEM image and *I–V* curve are shown in Fig. S4 (ESI†).[57] The IPCE comparison between these two kinds of structures is demonstrated in Fig. 6. In this figure the 250 nm sized IOS α-Fe_2O_3 electrode with 9 minutes electrodeposition at 400 °C is compared with the corresponding

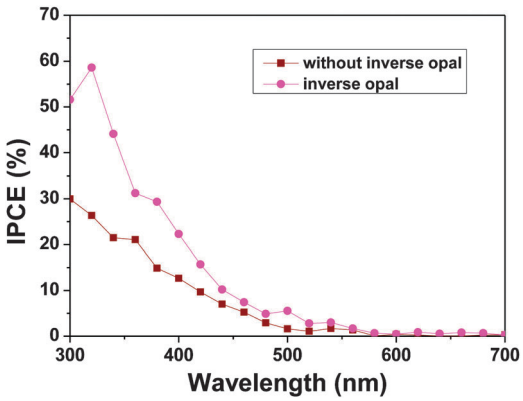

Fig. 6 IPCE of the inverse opal structure and general structure α-Fe_2O_3 checked at 0.5 V *vs.* Ag/AgCl in 1 M NaOH electrolyte.

general structured α-Fe_2O_3 electrode. The IPCE data shows a maximum value between 350 to 380 nm, and the photoresponse range is extended to about 600 nm, which is consistent with the previous report.[10] The maximum IPCE value of the IOS α-Fe_2O_3 electrode is much higher than that of general structured α-Fe_2O_3 electrode.[57,58]

The IOS α-Fe_2O_3 electrodes used for solar water splitting have several important requirements of which were investigated by varying preparation conditions in this study. Firstly, the electrodes with a suitable 7 μm thickness could minimize the effect of rapid electron–hole recombination due to a relative short diffusion length. Secondly, the electrodes with 250 nm sized holes could produce a high surface to volume ratio and unique optical properties. Thirdly, the electrodes made under 400 °C annealing temperature could yield high ordered crystalline structure and keep the face-centered-cubic skeleton, by which the charge mobility is enhanced.[59,60]

Conclusions

According to the results mentioned above, the electrochemical process, as a novel technology, can be used as a way of constructing inverse opal structured α-Fe_2O_3 photoanodes. The easy-to-control electrochemical process preformed the geometry based on thickness, pore volume and interconnected skeleton, which significantly influenced the photoelectrochemical properties of the IOS α-Fe_2O_3. As a result, the IOS α-Fe_2O_3 sample with 250 nm holes, 7 μm thickness and annealing at 400 °C showed the highest photocurrent density. In addition, the taking advantages of the inverse opal structure for α-Fe_2O_3 electrode indicated that it can greatly shorten the distance for photogenerated holes and enhance light harvesting. Our systematic work demonstrated that the surface morphology and crystalline structure can have a significant effect on the photoelectrochemical properties and we believed that it can provide an in-depth foundation to improve the performance of hematite-based PEC cells.

Acknowledgements

This work was supported by an NRF grant funded by the Korea Ministry of Education, Science and Technology (MEST) (2011-0030254, 2013014038). J. H. Park acknowledges the Seoul 'R&D Program'.

Notes and references

1 A. Fujishima and K. Honda, *Nature*, 1972, **238**, 37–38.
2 K. Maeda, *J. Photochem. Photobiol., C*, 2011, **12**, 237–268.
3 A. J. Bard and M. A. Fox, *Acc. Chem. Res.*, 1995, **28**, 141–145.
4 M. Gratzel, *Nature*, 2001, **414**, 338–344.
5 M. G. Walter, E. L. Warren, J. R. McKone, S. W. Boettcher, Q. X. Mi, E. A. Santori and N. S. Lewis, *Chem. Rev.*, 2010, **110**, 6446–6473.
6 T. Ohmori, H. Takahashi, H. Mametsuka and E. Suzuki, *Phys. Chem. Chem. Phys.*, 2000, **2**, 3519–3552.
7 Y. C. Ling, G. M. Wang, D. A. Wheeler, J. Z. Zhang and Y. Li, *Nano Lett.*, 2011, **11**, 2119–2125.
8 K. Sivula, R. Zboril, F. L. Formal, R. Robert, A. Weidenkaff, J. Tucek, J. Frydrych and M. Gratzel, *J. Am. Chem. Soc.*, 2010, **132**, 7436–7444.
9 A. M. Mao, G. Y. Han and J. H. Park, *J. Mater. Chem.*, 2010, **20**, 2247–2250.
10 Y. J. Lin, S. Zhou, S. W. Sheehan and D. W. Wang, *J. Am. Chem. Soc.*, 2011, **133**, 2398–2401.
11 S. M. Ahrned, J. Leduc and S. F. Haller, *J. Phys. Chem.*, 1988, **92**, 6655–6660.
12 K. Sivula, F. L. Formal and M. Gratzel, *ChemSusChem*, 2011, **4**, 432–449.
13 M. P. Dare-Edwards, J. B. Goodenough, A. Hamnett and P. R. Ravellick, *J. Chem. Soc., Faraday Trans. 1*, 1983, **79**, 2027–2031.
14 A. Hagfeldt, U. Bjorksten and M. Gratzel, *J. Phys. Chem.*, 1996, **100**, 8045–8048.
15 Y. S. Hu, A. Kleiman-Shwarsctein, A. J. Forman, D. Hazen, J. N. Park and E. W. McFarland, *Chem. Mater.*, 2008, **20**, 3803–3805.
16 A. Watanabe and H. Kozuka, *J. Phys. Chem. B*, 2003, **107**, 12713–12720.
17 U. Bjorksten, J. Moser and M. Gratzel, *Chem. Mater.*, 1994, **6**, 858–863.
18 A. Duret and M. Gratzel, *J. Phys. Chem. B*, 2005, **109**, 17184–17191.
19 A. Kay, I. Cesar and M. Gratzel, *J. Am. Chem. Soc.*, 2006, **128**, 15714–15721.
20 Y. S. Hu, A. Kleiman-Shwarsctein, A. J. Forman, G. D. Stucky and E. W. McFarland, *J. Phys. Chem. C*, 2008, **112**, 15900–15907.
21 W. B. Ingler and S. U. M. Khan, *Int. J. Hydrogen Energy*, 2005, **30**, 821–827.
22 N. T. Hahn and C. B. Mullins, *Chem. Mater.*, 2010, **22**, 6474–6482.
23 Y. Q. Song, S. S. Qin, Y. W. Zhang, W. Q. Gao and J. P. Liu, *J. Phys. Chem. C*, 2010, **114**, 21158–21164.
24 R. Morrish, M. Rahman, J. M. D. MacElroy and C. A. Wolden, *ChemSusChem*, 2011, **4**, 474–479.
25 T. Lindgren, H. L. Wang, N. Beermann, L. Vayssieres, A. Hagfeldt and S. E. Lindquist, *Sol. Energy Mater. Sol. Cells*, 2002, **71**, 231–243.
26 A. M. Mao, K. H. Shin, J. K. Kim, D. H. Wang, G. Y. Han and J. H. Park, *ACS Appl. Mater. Interfaces*, 2011, **3**, 1852–1858.
27 F. L. Formal, M. Gratzel and K. Sivula, *Adv. Funct. Mater.*, 2010, **20**, 1099–1107.
28 E. S. Kwak, W. Lee, N. G. Park, J. Kim and H. Lee, *Adv. Funct. Mater.*, 2009, **19**, 1093–1099.
29 S. Nishimura, N. Abrams, B. A. Lewis, L. I. Halaoui, T. E. Mallouk, K. D. Benkstain, J. V. De Lagemaat and A. J. Frank, *J. Am. Chem. Soc.*, 2003, **125**, 6306–6310.
30 S. S. Huttner, M. Kolle, M. E. Welland, P. Muller-Buschbaum, R. H. Friend, U. Steiner and N. Tètreault, *Nano Lett.*, 2010, **10**, 2303–2309.
31 L. J. Liu, S. K. Karuturi, L. T. Su and A. I. Y. Tok, *Energy Environ. Sci.*, 2011, **4**, 209–215.

32 A. Mihi, C. J. Zhang and P. V. Braun, *Angew. Chem., Int. Ed.*, 2011, **50**, 5712–5715.
33 M. E. Harakeh and L. Halaoui, *J. Phys. Chem. C*, 2010, **114**, 2806–2813.
34 T. Suezaki, P. G. O'Brien, J. I. L. Chen, E. Loso, N. P. Kherani and G. A. Ozin, *Adv. Mater.*, 2009, **21**, 559–563.
35 C. W. Cheng, S. K. Karuturi, L. J. Liu, J. P. Liu, H. X. Li, L. T. Su, A. I. Y. Tok and H. J. Fan, *Small*, 2012, **8**, 37–42.
36 J. E. G. J. Wijnhoven and W. L. Vos, *Science*, 1998, **281**, 802–804.
37 A. Stein, F. Li and N. R. Denny, *Chem. Mater.*, 2008, **20**, 649–666.
38 P. G. O'Brien, N. P. Kherani, S. Zukotynski, G. A. Ozin, E. Vekris, N. Tetreault, A. Chutinan, S. John, A. Mihi and H. Miguez, *Adv. Mater.*, 2007, **19**, 4177–4182.
39 Q. Li and J. K. Shang, *J. Am. Ceram. Soc.*, 2008, **91**, 660–663.
40 J. Liu, G. L. Liu, M. Z. Li, W. Z. Shen, Z. Y. Liu, J. X. Wang, J. C. Zhao, L. Jiang and Y. L. Song, *Energy Environ. Sci.*, 2010, **3**, 1503–1506.
41 F. Sordello, C. Duca, V. Maurino and C. Minero, *Chem. Commun.*, 2011, **47**, 6147–6149.
42 K. Shin, J. H. Moon and J. H. Park, *J. Nanosci. Nanotechnol.*, 2011, **11**, 1538–1541.
43 J. W. Goodwin, J. Hearn, C. C. Ho and R. H. Ottewill, *Colloid Polym. Sci.*, 1974, **252**, 464–471.
44 F. Sordello, V. Maurino and C. Minero, *J. Mater. Chem.*, 2011, **21**, 19144–19152.
45 D. K. Bora, A. Braun, R. Erni, G. Fortunato, T. Graule and E. C. Constable, *Chem. Mater.*, 2011, **23**, 2051–2061.
46 F. L. Souza, K. P. Lopes, E. Longo and E. R. Leite, *Phys. Chem. Chem. Phys.*, 2009, **11**, 1215–1219.
47 R. H. Goncalves, B. H. R. Lima and E. R. Leite, *J. Am. Chem. Soc.*, 2011, **133**, 6012–6019.
48 N. T. Hahn, H. C. Ye, D. W. Flaherty, A. J. Bard and C. B. Mullins, *ACS Nano*, 2010, **4**, 1977–1986.
49 M. Sorescu, R. A. Brand, D. Mihaila-Tarabasanu and L. Diamandescu, *J. Appl. Phys.*, 1999, **85**, 5546–5548.
50 Y. Wang, S. Wang, W. Zhao, B. Zhu, F. Kong, D. Wang, S. Wu, W. Huang and S. Zhang, *Sens. Actuators, B*, 2007, **125**, 79–84.
51 T. C. Lin, G. Seshadri and J. A. Kelber, *Appl. Surf. Sci.*, 1997, **119**, 83–92.
52 A. M. Mao, N. G. Park, G. Y. Han and J. H. Park, *Nanotechnology*, 2011, **22**, 175703(1–7).
53 M. K. Wu, T. Ling, Y. Xie, X. G. Huang and X. W. Du, *Semicond. Sci. Technol.*, 2011, **26**, 105001.
54 Y. X. Shi, H. J. Wang and N. S. Cai, *J. Power Sources*, 2012, **208**, 24–34.
55 Y. X. Shi, N. S. Cai, C. Li, C. Bao, E. Croiset, J. Q. Qian, Q. Hu and S. R. Wang, *J. Electrochem. Soc.*, 2008, **155**, B270–B280.
56 B. L. He, B. Dong and H. L. Li, *Electrochem. Commun.*, 2007, **9**, 425–430.
57 Y. J. Lin, G. B. Yuan, S. Sheehan, S. Zhou and D. W. Wang, *Energy Environ. Sci.*, 2011, **4**, 4862–4869.
58 M. J. Katz, S. C. Riha, N. C. Jeong, A. B. F. Martinson, O. K. Farha and J. T. Hupp, *Coord. Chem. Rev.*, 2012, **256**, 2521–2529.
59 K. Zhang, X. Shi, J. K. Kim, J. S. Lee and J. H. Park, *Nanoscale*, 2013, **5**, 1939–1944.
60 D. Y. Kang, Y. Lee, C. Y. Cho and J. H. Moon, *Langmuir*, 2012, **28**, 7033–7038.

